NASA Technical Memorandum 100042

Navier-Stokes Simulation of Wind-Tunnel Flow Using LU-ADI Factorization Algorithm

Shigeru Obayashi, Kozo Fujii and Sharad Gavali

February 1988

NASA
National Aeronautics and
Space Administration

Navier-Stokes Simulation of Wind-Tunnel Flow Using LU-ADI Factorization Algorithm

Shigeru Obayashi
Kozo Fujii, Ames Research Center, Moffett Field, California

Sharad Gavali, Amdahl Corporation, Sunnyvale, California

NASA

NAVIER-STOKES SIMULATION OF WIND-TUNNEL FLOW USING LU-ADI FACTORIZATION ALGORITHM

Shigeru Obayashi
Kozo Fujii *
NASA Ames Research Center, Moffett Field, California, USA
Sharad Gavali
Amdahl Corporation, Sunnyvale, California, USA

SUMMARY

The three-dimensional Navier-Stokes solution code using the LU-ADI factorization algorithm was employed to simulate the workshop test cases of transonic flow past a wing model in a wind tunnel and in free air. The effects of the tunnel walls are well demonstrated by the present simulations. An Amdahl 1200 supercomputer having 128 Mbytes main memory was used for these computations.

INTRODUCTION

Computational Fluid Dynamics (CFD) is achieving a status comparable to classical methods of laboratory experiment and theoretical analysis. The foremost tools of CFD researchers are supercomputers. With the available huge memory of these machines, it is now possible to solve the compressible Navier-Stokes equations using a large number of grid points.

Since the use of a supercomputer is one of the important factors for practical Navier-Stokes simulations, the solution algorithm which is used should have good vectorization capability in addition to efficiency and robustness. Efforts have been made by the authors and many scientists to develop such algorithms, and a number of results using supercomputers have been reported recently [1-3]. The present authors also have been engaged in developing an efficient and robust three-dimensional Navier-Stokes code. The LU-ADI algorithm used in the code was originally developed by Obayashi and Kuwahara [4] for the two-dimensional problem. Extension to three dimensions and

---

* Present address: National Aerospace Laboratory, Tokyo, Japan.

application to relatively simple geometries were reported in reference 5. A series of studies [6-10] for practical applications of the code to transonic flow over transport aircraft configurations have been done in parallel with improvements in stability and efficiency.

In the present paper, computations for the workshop test problems were carried out by using the three-dimensional Reynolds-averaged "thin-layer" Navier-Stokes equations. The turbulent eddy viscosity was computed by using the Baldwin-Lomax model modified for two thin layers [11]; that is, for the wing surface and wind-tunnel walls.

The LU-ADI factorization algorithm was used to obtain the steady-state solution. Computations were carried out for 0 and 2° angle-of-attack cases for the wing in the wind tunnel, and for 0, 2, 5 and 8° angle-of-attack cases for an isolated wing with the free-stream Mach number and Reynolds number corresponding to the experiment [12]. An Amdahl 1200 supercomputer was used for the computations. For the wind-tunnel simulation, the CPU time was 10.0 μ sec/step/grid point, and the required memory was 92 Mbytes for about 0.8 million grid points.

GOVERNING EQUATIONS AND NUMERICAL ALGORITHM

Compressible Navier-Stokes Equations

The partial differential equations governing the three-dimensional compressible viscous flow of an ideal gas are the compressible Navier-Stokes equations. Written here in the conservation-law form and in the generalized coordinates, they are given by,

$$\partial_\tau \widehat{Q} + \partial_\xi \widehat{E} + \partial_\eta \widehat{F} + \partial_\varsigma \widehat{G} = Re^{-1}(\partial_\eta \widehat{S}_1 + \partial_\varsigma \widehat{S}_2). \tag{1}$$

For high Reynolds-number flows, the viscous effects are confined to a thin layer near wall boundaries and are dominated by the viscous terms associated with the strain rates normal to the surface. The terms associated with the strain rates along the surface are comparatively small and negligible. Also, since the computational grid is highly concentrated near the surface and, as a result, the mesh aspect ratio becomes very large, inclusion of these terms would not change the solution. Thus, the thin-layer approximation has been introduced in equation (1) as is typically done in most Navier-

Stokes computations. In addition, the thin-layer approximation has been extended to two directions in equation (1) since viscous layers must be considered on both the wing and the wing root at a side wall. The cross-derivative terms are neglected and only $\widehat{S}_{1\eta}$ and $\widehat{S}_{2\varsigma}$ terms are retained.

The pressure, density, and velocity components are related to the internal energy for an ideal gas as follows,

$$p = (\gamma - 1)(e - \rho(u^2 + v^2 + w^2)/2). \tag{2}$$

In the following computations, the viscosity coefficient in equation (1) is computed as the sum of $\mu + \mu_t$. The turbulent eddy viscosity, μ_t, is computed by using the two-layer algebraic eddy viscosity Baldwin-Lomax model with a modified length scale. The length scales are difficult to define near the junction of a fuselage and a wing. In the present study, the evaluation of length scales proposed by Hung and Buning for their blunt-fin study [11] is adopted.

The metrics are evaluated using second-order central-difference formulas for interior-points, and three-point, one-sided formulas at the boundaries. The steady-state solution of equation (1) is obtained by time integration in a time-asymptotic fashion.

LU-ADI Factorization Algorithm

The time-marching method used here is the LU-ADI factorization proposed by the present authors [8]. Implicit time-integration methods with a delta form are widely used for solving steady-state problems since the steady-state solution is independent of the left-hand side operators. The most commonly used is the ADI factorization Beam and Warming method used in reference 13. The present LU-ADI factorization method is a compromise of ADI and LU factorization [14]. Each ADI operator is decomposed into the product of lower and upper bidiagonal matrices by using a flux vector-splitting technique [15] and a diagonally dominant factorization [16].

It should be noted that the right-hand side of the equation remains in the form of central differencing and numerical smoothing similar to the Beam-Warming method. For the convective terms on the right-hand side, fourth-order differencing is used except near the boundaries. Maintenance of the free stream is achieved by subtracting the

free-stream fluxes from the governing equations. As a result, the present scheme is first order in time and second order in space.

The present method applied to equation (1) is written as,

$$T_\xi L_A D_A U_A T_\xi^{-1} T_\eta L_B D_B U_B T_\eta^{-1} T_\varsigma L_C D_C U_C T_\varsigma^{-1} \Delta \widehat{Q}^n$$
$$= -h\{\delta_\xi \widehat{E}^n + \delta_\eta \widehat{F}^n + \delta_\varsigma \widehat{G}^n - Re^{-1}(\delta_\eta^2 \widehat{S}_1^n + \delta_\varsigma^2 \widehat{S}_2^n)\}$$
$$+(D_e|_\xi + D_e|_\eta + D_e|_\varsigma)\widehat{Q}^n \tag{3}$$

where h is the time step, δ is a central finite-difference operator, and D_e is the explicit nonlinear artificial dissipation operator. On the left-hand side, the original ADI operator of the Beam-Warming method is rewritten using the diagonal form [17] and the flux vector splitting technique [15]. For example, in the ξ direction,

$$I + h\delta_\xi \widehat{A}$$
$$= T_\xi (I + h\delta_\xi^b \widehat{D}_A^+ + h\delta_\xi^f \widehat{D}_A^-) T_\xi^{-1}$$
$$= T_\xi (I - \alpha h \widehat{D}_{Aj}^- + h\delta_\xi^b \widehat{D}_A^+)(I + \alpha h |\widehat{D}_{Aj}|)^{-1}(I + \alpha h \widehat{D}_{Aj}^+ + h\delta_\xi^f \widehat{D}_A^-) T_\xi^{-1}$$
$$= T_\xi L_A D_A U_A T_\xi^{-1} \tag{4}$$

where α is a coefficient appearing at the diagonal elements for the upwind differencing. In other words, $\alpha = 1$ when first-order differencing is used for the ξ-derivative, and $3/2$ when second-order differencing is used. Currently, α is set to be $7/6$ since three-point first-order differencing is used for the ξ-derivative to be consistent with fourth-order differencing in the right-hand side convective terms. The decomposition used in equation (4) is the approximate LDU factorization. This decomposition is more stable than simple LU factorization since the diagonal element always has the absolute value of the eigenvalues.

In the solution process, an inversion in one direction consists of one scalar forward sweep and one scalar backward sweep. Thus, the LU-ADI algorithm requires little additional memory and is easily vectorized. It may be noteworthy that LDU operator can be regarded as a symmetric Gauss-Seidel relaxation.

The split eigenvalues in each direction, $\widehat{D}_A^\pm$, $\widehat{D}_B^\pm$ and $\widehat{D}_C^\pm$, are modified corresponding to the implicit artificial dissipation terms and the viscous terms [5].

Nonlinear Artificial Dissipation Model

The fourth-order dissipation model has been widely used with central differencing in Navier-Stokes computations [3,5,13]. On the other hand, the second-order dissipation produced by proper upwinding works better than the fourth-order dissipation model in regions near discontinuities. Such dissipation, however, is not desirable for the rest of the flow field since it reduces the spatial accuracy to at most first order. Higher-order TVD upwind schemes can be constructed by introducing flux limiters [18,19].

A numerical flux for first-order upwind differencing of the convective terms can be written as

$$F_{j+1/2} = (F_j + F_{j+1})/2 - dF^a_{j+1/2}/2 \qquad (5)$$

where $dF^a_{j+1/2} = |A_{j+1/2}|(Q_{j+1} - Q_j)$. Introducing a flux limiter Φ to obtain second-order central differencing, equation (5) is rewritten as,

$$F_{j+1/2} = (F_j + F_{j+1})/2 - (I - \Phi)dF^a_{j+1/2}/2. \qquad (6)$$

To construct the present dissipation model, a simplified model of a flux is considered. The matrix, $|A_{j+1/2}|$ is replaced by the spectral radius $\sigma_\xi = |U| + cr_\xi$ so that the artificial dissipation terms can be simply evaluated;

$$d\widehat{F}^\sigma_{j+1/2} = (\sigma_\xi/J)_{j+1/2}(J\widehat{Q}_{j+1} - J\widehat{Q}_j) \qquad (7)$$

where the scaled spectral radius σ_ξ/J at $j + 1/2$ is taken as an arithmetic average at j and $j + 1$. This simple form may badly diffuse solutions even with the limiter. A small constant ε is introduced to the present model as well as conventional smoothing terms. A fourth-order dissipation term is also necessary to keep global stability to the central differencing. The final form of the present model is written as a combination of second- and fourth-order smoothing terms similar to an existing nonlinear model [17].

$$D_e|_\xi \widehat{Q} = \varepsilon h \nabla_\xi ((I - \Phi_{j+1/2})d\widehat{F}^\sigma_{j+1/2} - \Phi_{j+1/2}\delta^2_\xi d\widehat{F}^\sigma_{j+1/2}) \qquad (8)$$

The limiter Φ can be defined as a scalar function for each element:

$$\phi_{j+1/2} = minmod(1, r^+, r^-) \qquad (9)$$

where $r^+ = df_{j-1/2}/df_{j+1/2}, r^- = df_{j+3/2}/df_{j+1/2}$, and ϕ and df are elements of Φ and $d\widehat{F}^\sigma$, respectively.

The present dissipation model was implemented only in the ξ direction where a strong discontinuity may appear. In the other directions, only the fourth-order dissipation term was used by setting Φ to be I in equation (8). Only the fourth-order dissipation terms were used on the left-hand side of equation (3).

RESULTS AND DISCUSSIONS

Wing in Wind Tunnel

The grid topology used here is of the C-H type with C-grid around the wing section and H-grid for the wing span. First, grid distributions in the y (spanwise) direction were determined. Then the geometry of each wing section was computed at each spanwise location by using the surface generator code E88F5 due to Sobieczky [12]. Finally, the C-grid system in the x-z plane was generated by using the two-dimensional algebraic technique for each wing section with outer boundaries fitted to the control-surface geometry. The grid was clustered near wall surfaces including the wing surface. The minimum spacing normal to surfaces was set to 5×10^{-5} of the tunnel dimension which is 1 meter. The grid for each wing section at a constant spanwise location consists of 201×51 points, and 75 planes are distributed in the spanwise direction for a total of 768,825 points, of which 161×55 points are distributed on the wing surface. Figure 1 shows three two-dimensional views of the grid system. Figure 2 shows the overall view of the wing and the tunnel walls with the typical pressure distributions. Two grid systems were generated, corresponding to the wing at 0 and 2° angle of attack.

The test wing of this workshop corresponds to a practical design configuration which causes problems with grid generation. First, both the wing tip and trailing edge of this wind-tunnel test model have thickness. Therefore, the surface grids in the wing extension and wake cut were closed at the next grid point from the tip and trailing edge, respectively. Next, the test model has a large curvature near the wing tip and root. Thus, orthogonality of the grid system was enforced only near the wing surface

in the x-z plane, not near the wing tip and root-side wall (not in the x-y plane and y-z plane).

The flow conditions consist of Mach number 0.82, Reynolds number 10 million based on the tunnel dimension $1m$, and 0 and $2°$ angles of attack. For turbulent flow calculations, the Baldwin-Lomax turbulence model modified for wing-wall configurations was used for the following four regions: the wing and the root-side wall, the wing extension (flow-through condition) and the other side wall, the lower or upper wall and the root-side wall, and the lower or upper wall and the other side wall. Two types of turbulent-flow computations were performed. One assumed fully turbulent flow and the other assumed transition to turbulent flow following experimental data provided by the Workshop Organizer. In total, four cases were computed for the wing in a wind tunnel. In the following computations, the subroutine for the turbulence model was called every 10 time steps to reduce CPU time, since the turbulence model computations represented 30% of the time required for one time step.

At the inflow boundary, all variables were fixed to experimental data given by the inlet and exit conditions code E17F5 [12]. At the outflow boundary, the pressure was fixed by using the code E17F5 and the other variables were extrapolated. No-slip and adiabatic wall conditions were used on both the wing surface and wind-tunnel walls. The pressure on the surfaces was obtained from the normal momentum equation. The initial conditions were obtained by assuming the inflow profiles of flow quantities in the y-z plane to remain unchanged in the x direction. Therefore, boundary-layer profiles were assumed on the tunnel walls as the initial condition, while the slow-start technique was used for the wing surface.

The CFL number was set to 20 initially and increased up to 400 during the first 1000 iterations. The smoothing coefficient ε started from 0.4 and decreased to 0.08 at the same time. To guarantee convergence, the computation was continued until the total time, nondimensionalized by the tunnel dimension and speed of sound, exceeded 4.5. This meant using over 6000 iterations because of the constraint of the time step at the wing root. Since CPU time/step/grid point was 10.0 μ sec, the total CPU time was about 13 hr for one case.

Figure 3 shows the computed results for the fully turbulent flow at $0°$ angle of attack. Figure 3a shows the coefficient of pressure at three spanwise locations, $2y/b = 0.2, 0.5$

and 0.8. The pressure-contour plots on the wing upper surface and the corresponding surface-flow pattern are shown in Fig. 3b and c. Two types of separation can be observed. One is the trailing-edge separation and the other is the spiral-like separation near the wing root. The latter is due to the interaction between the boundary layers on the wing surface and the side wall. Figure 3d shows the pressure-contour plots on the lower and upper walls. Both plots coincide with each other because of 0° angle of attack.

Figure 4 shows corresponding plots for fully turbulent flow at 2° angle of attack. In Fig. 4c, the surface-flow pattern indicates occurrence of shock-induced separation. This separation line is almost straight in the mid-span region, then turns to the trailing edge near the wing tip where the shock wave becomes weaker, and turns to the upstream. Flow separation at the wing root is also observed. The effect of angle of attack is apparent from the contour plots even on the lower and upper tunnel walls as shown in Fig. 4d.

Two discrepancies can be pointed out in Figs. 3d and 4d. One is a steep rise of pressure near the inflow boundary, $x = -0.3$. The given inflow data specified only the boundary-layer velocity profile. Since density and temperature were assumed to be uniform at the inflow boundary, the numerical solutions changed rapidly to overcome this inconsistency. Density or temperature profiles will be required to obtain well-defined inflow data. (Pressure alone is not sufficient to define the boundary-layer properties.)

The other discrepancy is the presence of kinks in the contours near the outflow boundary. There is a large pressure gradient in the y direction at the outflow boundary, $x = 0.63$, which is caused by the splitter plate (root-side wall) [20]. The pressure profiles obtained by experiment showed only two-dimensional profiles varying in the y direction and did not show the effect of changing angle of attack. But the numerical results indicate three dimensionality and the effect of changing angle of attack (for example at $x = 0.5$ in Figs. 3d and 4d), even though the effects are less than that caused by the splitter plate. More precise data will be required to specify the pressure profiles at the outflow boundary.

Figures 5 shows corresponding plots for the transitional flow at 0° angle of attack. The pressure gradient on the wing surface is more moderate near the wing root when

compared with the fully turbulent flow case. Thus, no trailing-edge separation is observed in Fig. 5c. The pressure contours in Fig. 5b have kinks along the transition line where the turbulence model was turned on as a step function.

Figure 6 shows the results of transitional flow at 2° angle of attack. Again, the pressure gradient on the wing surface is more moderate near the wing root in Fig. 6b and the flow is attached in Fig. 6c. However, the shock wave appears to be stronger and thus induces flow separation at mid span.

Flow-separation patterns are different for the fully turbulent flow case and the transitional flow case. Profiles of u-velocity are plotted in Fig. 7. The flow appears to accelerate in the laminar flow region for the transitional flow case, while the fully turbulent flow leads to a thick boundary layer.

Isolated Wing in Free Air

The grid system for the isolated wing was generated in the same way as for the wing in a wind tunnel. The spanwise grid distributions were taken from default of the code E88F5 as 40 points on the wing with ten points added for the wing extension and one additional point for implementing the symmetry condition at the wing root. Then C-grids of 201×51 points were generated at each spanwise station, with outer boundaries located 10 chord away. The minimum spacing normal to the wing surface was set to 5×10^{-5} of each chord length. The number of grid points on the wing surface was 151×41 points. The total number of grid points was $201 \times 51 \times 51$; that is, 522,801 points. The same grid system was used for different angle-of-attack cases.

The flow conditions consist of Mach number 0.82, Reynolds number 10 million based on the reference length of $1m$, and 0, 2, 5, and 8° angles of attack. The flow was assumed as fully turbulent. For the boundary conditions, free-stream values were specified at the far-field boundary. At the outflow boundary, the pressure was fixed to the free-stream value and the other variables were extrapolated. The slow-start technique was used to start iterations.

Figure 8 shows the chordwise pressure distributions at $2y/b = 0.2$, 0.5 and 0.8 for four angle-of-attack cases, respectively. Figure 9 shows the pressure-contour plots on the upper surface of the wing. The suction peaks appear to be lower in the free-air

case compared with the corresponding wind-tunnel case. For the wind-tunnel cases, however, the suction peak becomes much higher on the lower surface (for example, compare Fig. 4a with Fig. 8b) since this is the pressure side in the wind tunnel. Therefore, the lift coefficient is larger for the free-air case even though the suction peaks are lower. Figure 10 shows the surface-flow patterns. No separation is observed at 0° angle-of-attack. The root separation observed in the wind-tunnel cases (because of the interaction of the side wall) did not occur for the free-air cases. At 2° angle-of-attack, the shock wave is weaker for the free-air case and thus the shock-induced separation is not observed. Large-scale separation is observed at higher angles of attack.

The lift coefficient C_L as a function of angle of attack α is shown in Fig. 11. The curve shows the nonlinearity at higher angles of attack. The lift coefficient obtained for fully turbulent flow computations at 2° angle of attack in the wind tunnel is smaller than that obtained in free air because of the existence of the tunnel walls. The transitional turbulence model causes differences in lift coefficients of about 15% for the wind-tunnel simulations. This indicates that improvements of turbulence modeling are needed for aerodynamic predictions even at moderate angles of attack. Figure 12 shows the drag polar. The free-air case produces the highest drag at 0° angle of attack here, since the boundary layer on the side wall for the wind-tunnel cases was not taken into account in the present force calculation. The fully turbulent flow cases result in higher total drag than the transitional flow cases.

CONCLUDING REMARKS

The Navier-Stokes simulation of transonic flow past a test wing in a wind tunnel and in free air was carried out using the LU-ADI factorization algorithm. The Baldwin-Lomax model was used under the assumption of the fully turbulent flow. The effects of the tunnel walls are well demonstrated by the present simulations. Lift coefficients predicted by the wind-tunnel simulation were lower than those by the free-air simulation.

The specified transition line from laminar to turbulent flow was also tried for the wind-tunnel case. This led to different results for the pressure distributions and the

separation patterns. In future, more work is required to simulate transitional flow correctly.

In addition, the grid-generation technique was not robust enough to treat complex geometry accurately, such as large curvature around the wing tip and root, and finite thickness at the wing tip and trailing edge. Further development is needed in this area.

Numerical results indicate that the accuracy of experimental data was insufficient to establish boundary conditions for computations. Both the inflow and outflow boundary profiles were insufficient to obtain smooth flow field profiles. More precise experimental data will be required for CFD validation.

ACKNOWLEDGMENT

REFERENCES

[1] FLORES, J., REZNICK, S. G., HOLST, T. L., GUNDY, K., "Navier-Stokes solutions for a fighter-like configuration," AIAA Paper 87-0032 (1987).

[2] KORDULLA, W., MacCORMACK R. W., "A new predictor-corrector scheme for the simulation of three-dimensional compressible flows with separation," AIAA Paper 85-1502 (1985).

[3] VADYAK, J., "Simulation of wing, fuselage, and wing/fuselage flowfield using a three-dimensional Euler/Navier-Stokes algorithm," AIAA Paper 85-1693 (1985).

[4] OBAYASHI, S., KUWAHARA, K., "An approximate LU factorization method for the compressible Navier-Stokes equations," J. Comp. Phys., *Vol. 63*, No. 1 (1986), pp. 157-167.

[5] OBAYASHI, S., FUJII, K.,"Computation of three-dimensional viscous transonic flows with the LU factored scheme," AIAA Paper 85-1510 (1985).

[6] OBAYASHI, S, MATSUSHIMA, K., FUJII, K., KUWAHARA, K., "Improvements in efficiency and reliability for Navier-Stokes computations using the LU-ADI factorization algorithm," AIAA Paper 86-0338 (1986).

[7] FUJII, K., OBAYASHI, S., "Navier-Stokes simulations of transonic flows over a practical wing configuration," AIAA J., *Vol. 25*, No. 3 (1987), pp. 369-370.

[8] FUJII, K., OBAYASHI, S., "Navier-Stokes simulation of transonic flows over wing-fuselage combinations," AIAA Paper 86-1831 (1986), to be published in AIAA Journal.

[9] OBAYASHI, S., FUJII, K., TAKANASHI, S., "Toward the Navier-Stokes analysis of transport aircraft configurations," AIAA Paper 87-0428 (1987).

[10] TAKANASHI, S., FUJII, K., OBAYASHI, S, MATSUSHIMA, K., "Numerical simulation of compressible viscous flows around practical aircraft configurations," AIAA Paper 87-2410 (1987).

[11] HUNG, C.-M., BUNING, P. G., "Simulation of blunt-fin induced shock wave and turbulent boundary-layer interaction," J. Fluid Mech., *Vol. 154* (1985), pp. 163-167.

[12] SOBIECZKY, H., "DFVLR-F5 test wing configuration for computational and experimental aerodynamics," preprint for workshop participants, IB 221 - 87 A 01 (1987).

[13] PULLIAM, T. H., STEGER, J. L.,"Implicit finite difference simulations of three-dimensional compressible flow," AIAA Journal, *Vol. 18*, No. 2 (1980), pp. 159-167.

[14] JAMESON, A., YOON, S., "Lower-upper implicit schemes with multiple grids for the Euler equations," AIAA Journal, *Vol. 25*, No. 7 (1987), pp. 929-935.

[15] STEGER, J. L., WARMING, R. F., "Flux vector splitting of the inviscid gasdynamic equations with application to finite-difference methods," J. Comp. Phys., *Vol. 40* (1981), pp. 263-293.

[16] LOMBARD, C. K., BARDINA, J., VENKATAPATHY, E., OLIGER, J., "Multidimensional formulation of CSCM - An upwind flux difference eigenvector split method for the compressible equations," AIAA Paper 83-1895 (1983).

[17] PULLIAM, T. H., STEGER, J. L., "Recent improvement in efficiency, accuracy, and convergence for implicit approximate factorization algorithms," AIAA Paper 85-360 (1985).

[18] SWEBY, P. K., "High resolution schemes using flux limiters for hyperbolic conservation laws," SIAM J. Numerical Anal., *Vol. 21*, No. 4 (1984), pp. 995-1011.

[19] ROE, P. L., "Generalized formulation of TVD Lax-Wendroff schemes," ICASE Report No. 84-53 (1984).

[20] SOBIECZKY, H., HEFER, G., TUSCHE, S., "DFVLR-F5 test wing experiment for computational aerodynamics," AIAA Paper 87-2485 (1987).

14
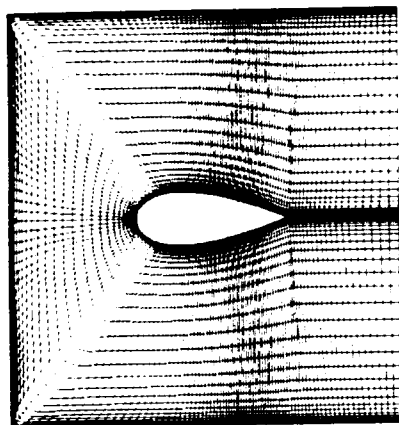
VIEW IN THE X-Z PLANE OF THE
WING ROOT
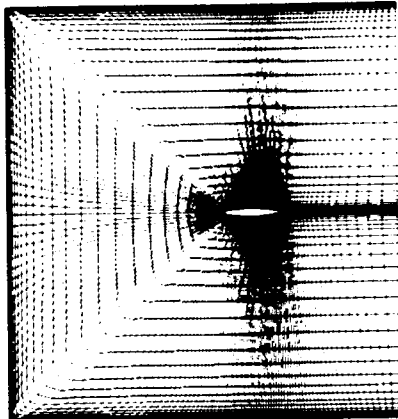
VIEW IN THE X-Z PLANE
2y/b = 0.5
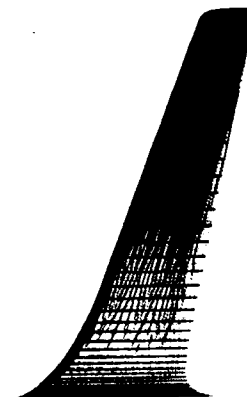
TOP VIEW OF THE
UPPER SURFACE OF
THE WING

Fig. 1 Grid distributions for wind-tunnel simulation.
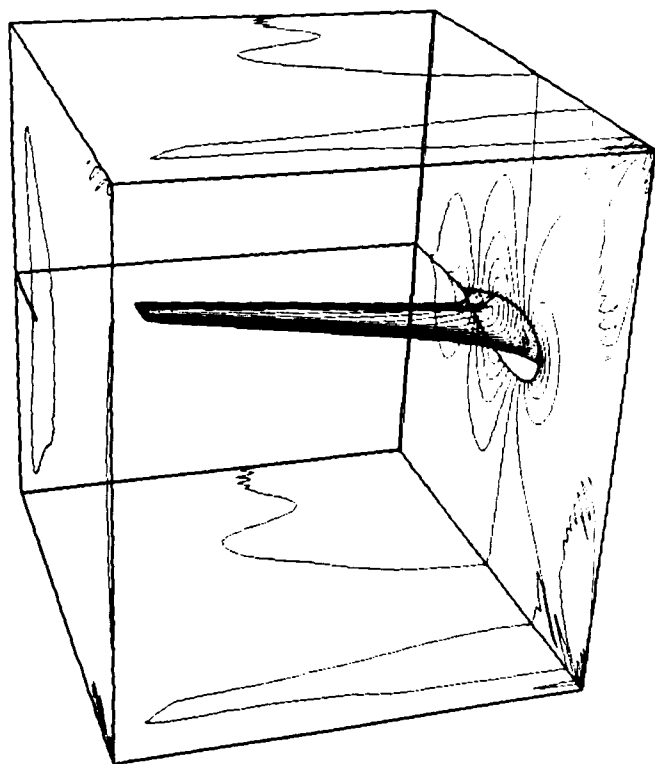
M_∞ = 0.82
R_e = 1.0 × 10^7
α = 0°

Fig. 2 Overall view of geometry and pressure distributions on surfaces.
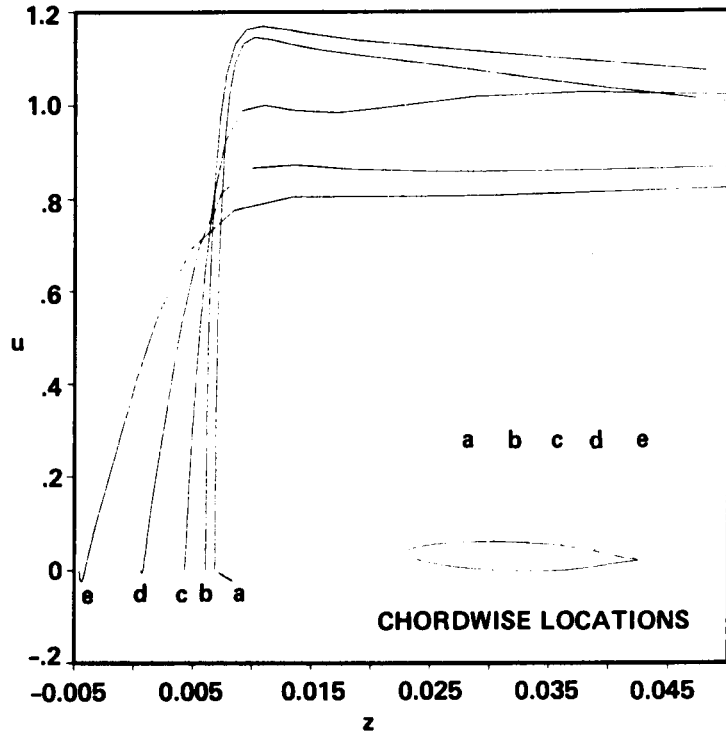
a) Chordwise pressure distributions.
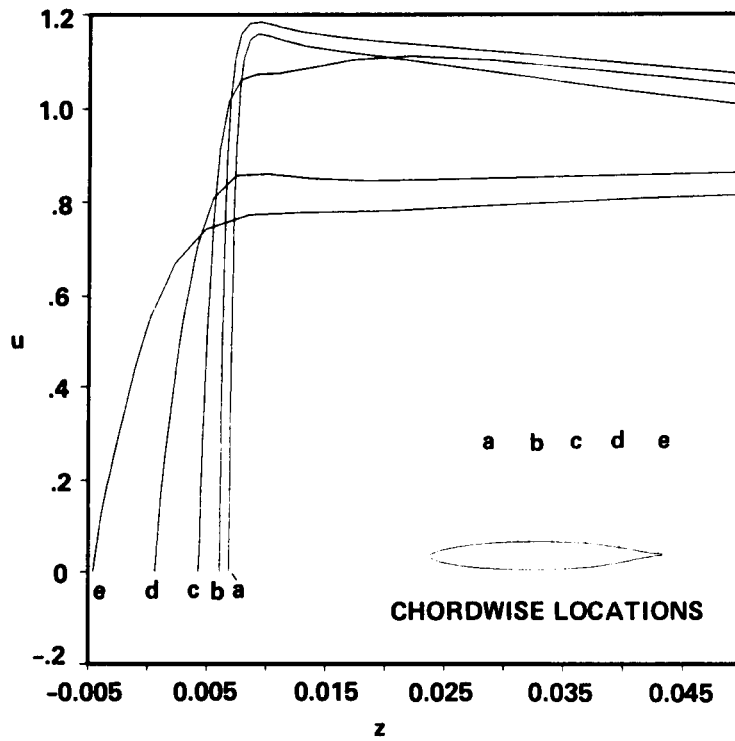
b) Pressure contour plots on wing upper surface.

c) Surface-flow pattern on wing upper surface.

Fig. 3 Computed results for $\alpha = 0°$ and fully turbulent flow case; $M_\infty = 0.82$, $Re = 1.0 \times 10^7$.

16

LOWER WALL   **UPPER WALL**
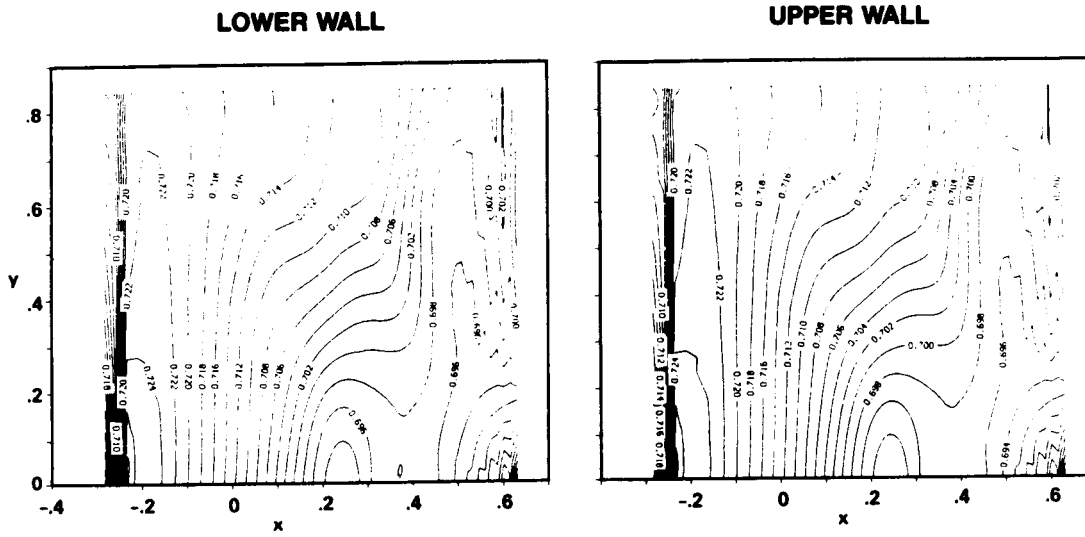
d) Pressure contour plots on lower and upper walls.

Fig. 3 Concluded.
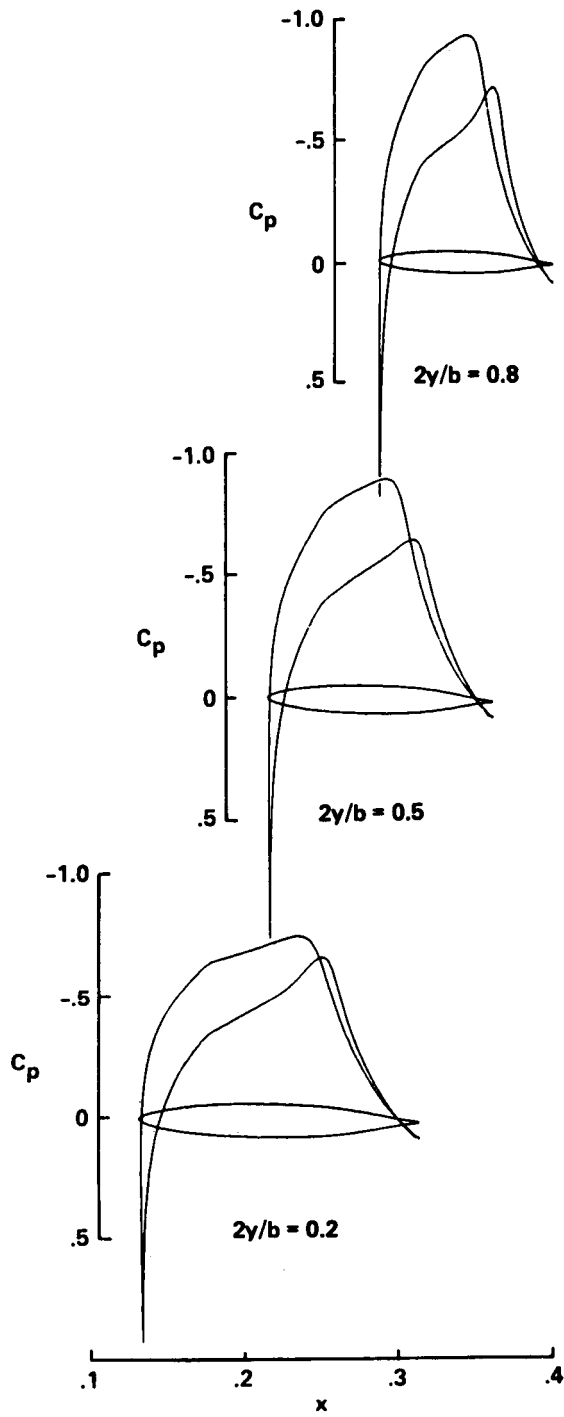
b) Pressure contour plots on wing upper surface.

a) Chordwise pressure distributions.
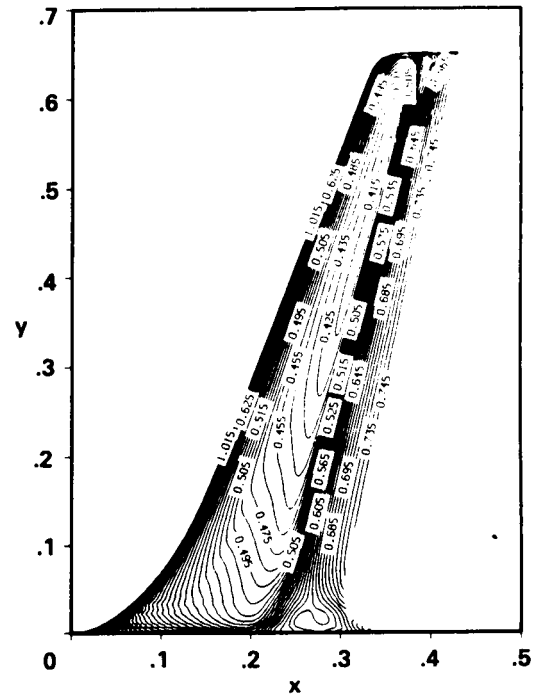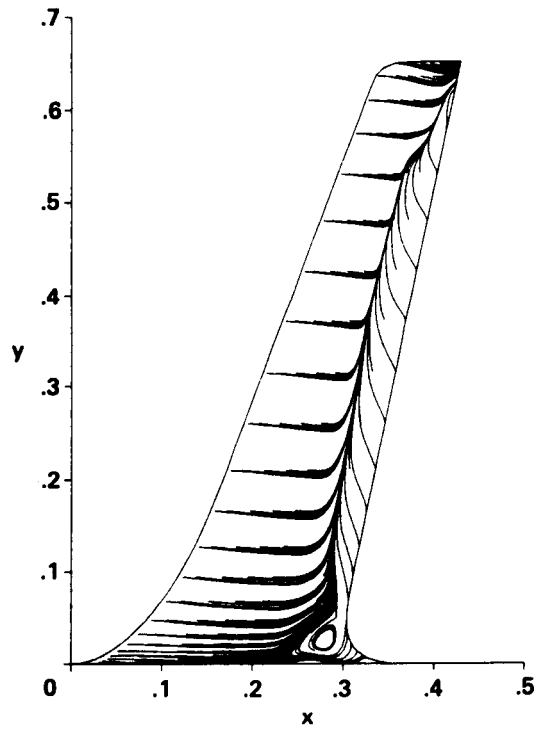
c) Surface-flow pattern on wing upper surface.

Fig. 4 Computed results for $\alpha = 2°$ and fully turbulent flow case; $M_\infty = 0.82$, $Re = 1.0 \times 10^7$.

18

LOWER WALL   **UPPER WALL**
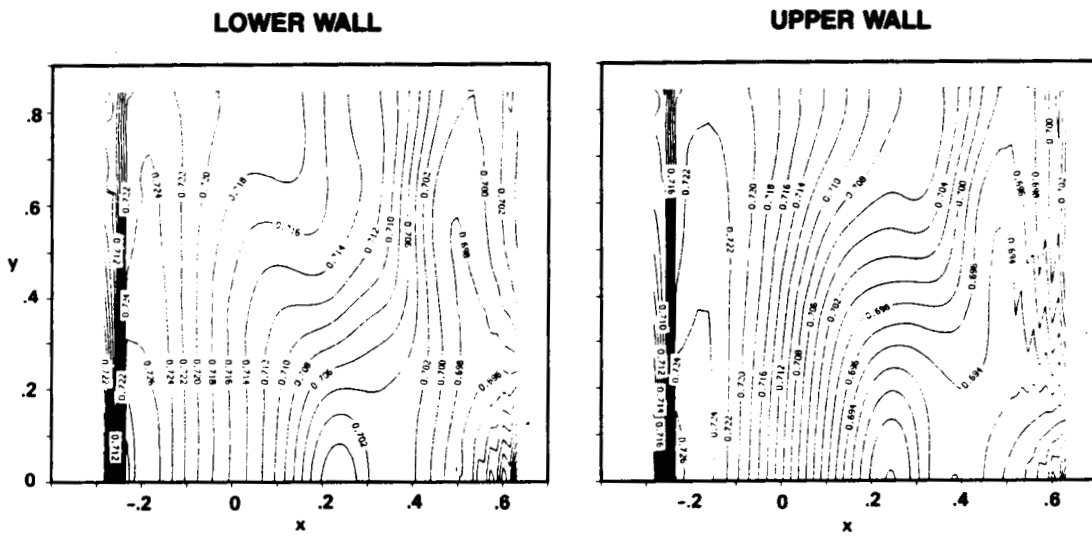
d) Pressure contour plots on lower and upper walls.

Fig. 4 Concluded.
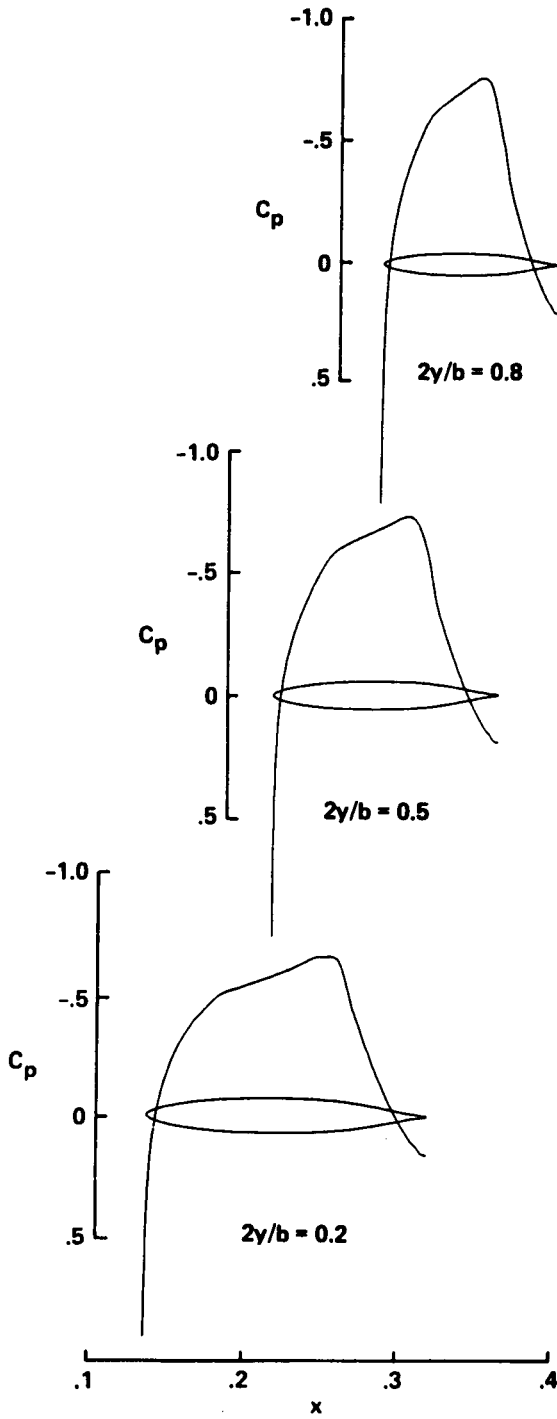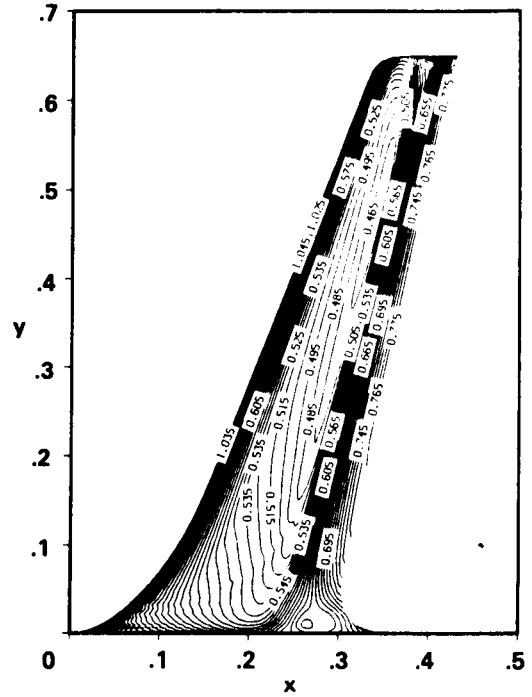
C_p

$2y/b = 0.8$

C_p

$2y/b = 0.5$

C_p

$2y/b = 0.2$

a) Chordwise pressure distributions.

b) Pressure contour plots on wing upper surface.
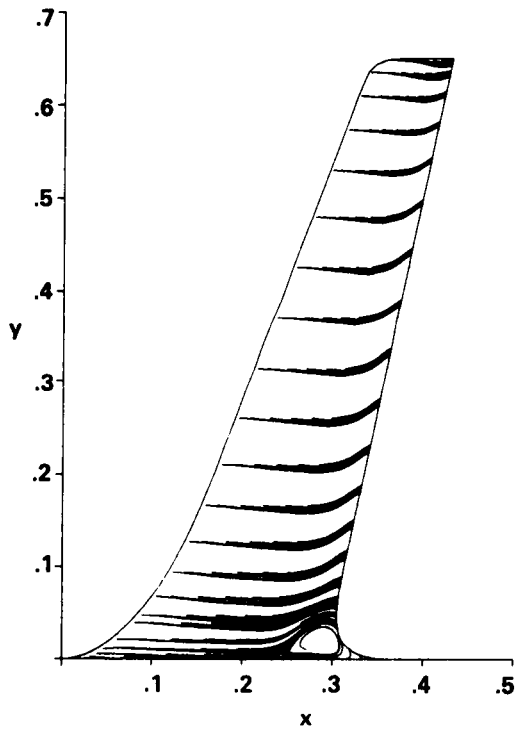
c) Surface-flow pattern on wing upper surface.

Fig. 5 Computed results for $\alpha = 0°$ and transitional flow case; $M_\infty = 0.82$, $Re = 1.0 \times 10^7$.
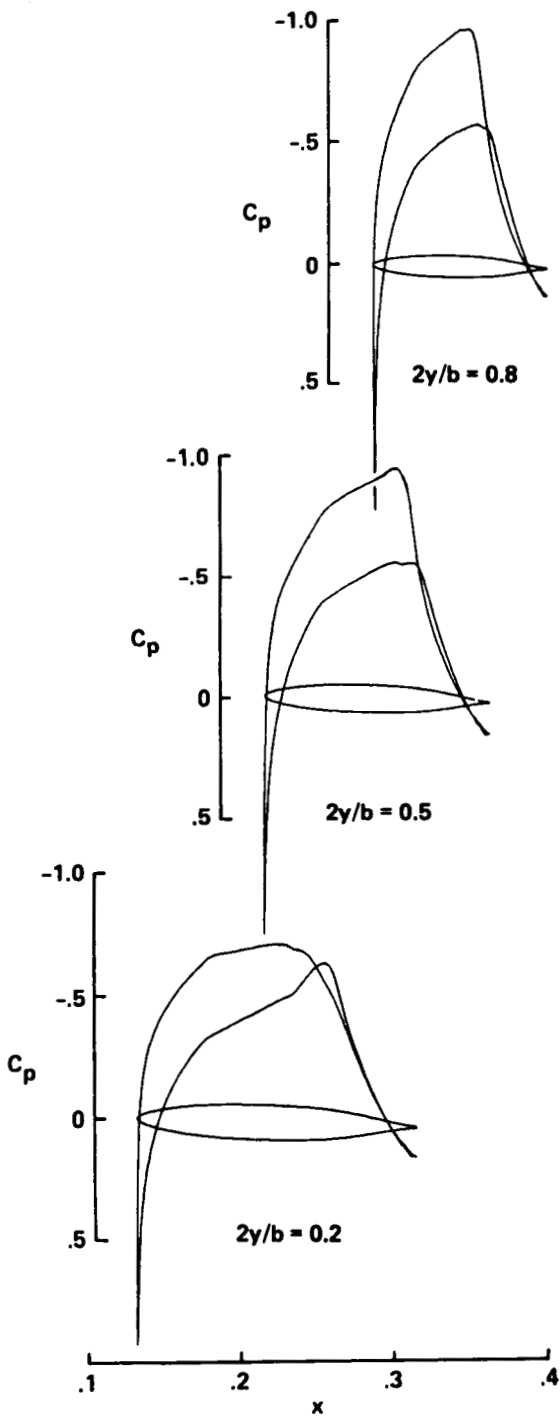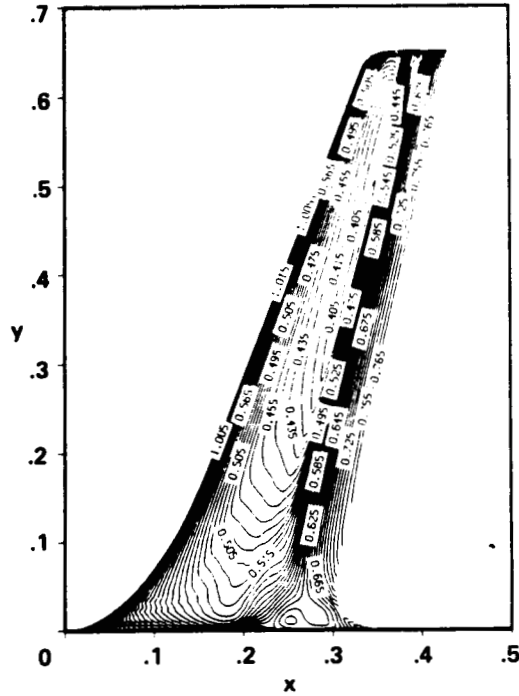
b) Pressure contour plots on wing upper surface.

a) Chordwise pressure distributions.
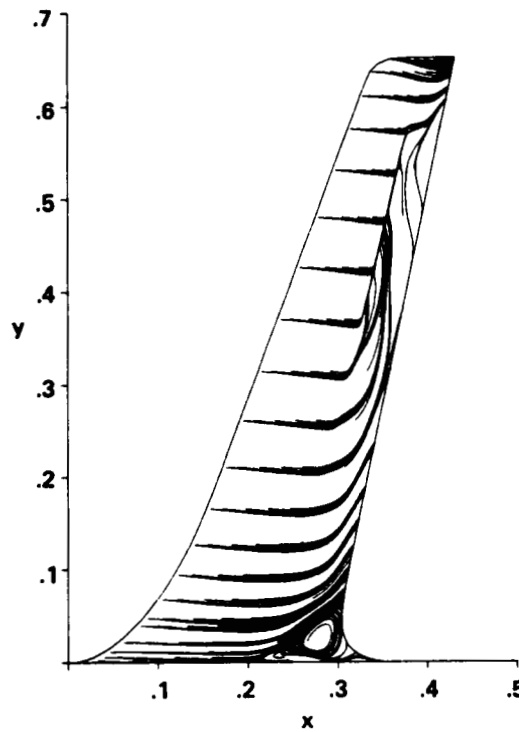
c) Surface-flow pattern on wing upper surface.

Fig. 6 Computed results for $\alpha = 2°$ and transitional flow case; $M_\infty = 0.82$, $Re = 1.0 \times 10^7$.

a) $\alpha = 2°$ and fully turbulent flow case.

b) $\alpha = 2°$ and transitional flow case.

Fig. 7 Profiles of u-velocity at several chordwise locations, $2y/b = 0.5$.

a) $\alpha = 0°$.

b) $\alpha = 2°$.
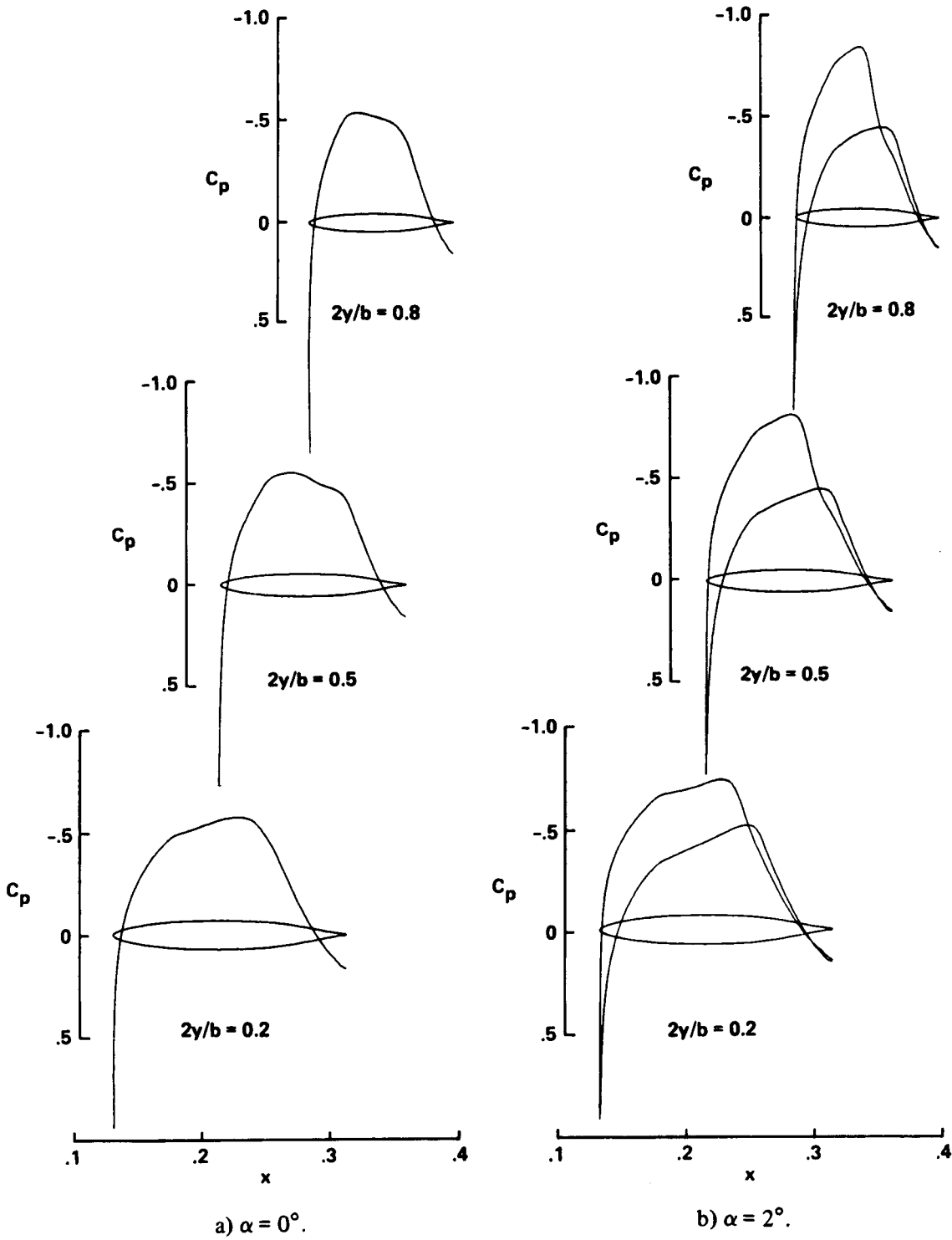
Fig. 8 Computed pressure distributions for isolated wing; $M_\infty = 0.82$, $Re = 1.0 \times 10^7$.

c) $\alpha = 5°$.

d) $\alpha = 8°$.

Fig. 8 Concluded.

24
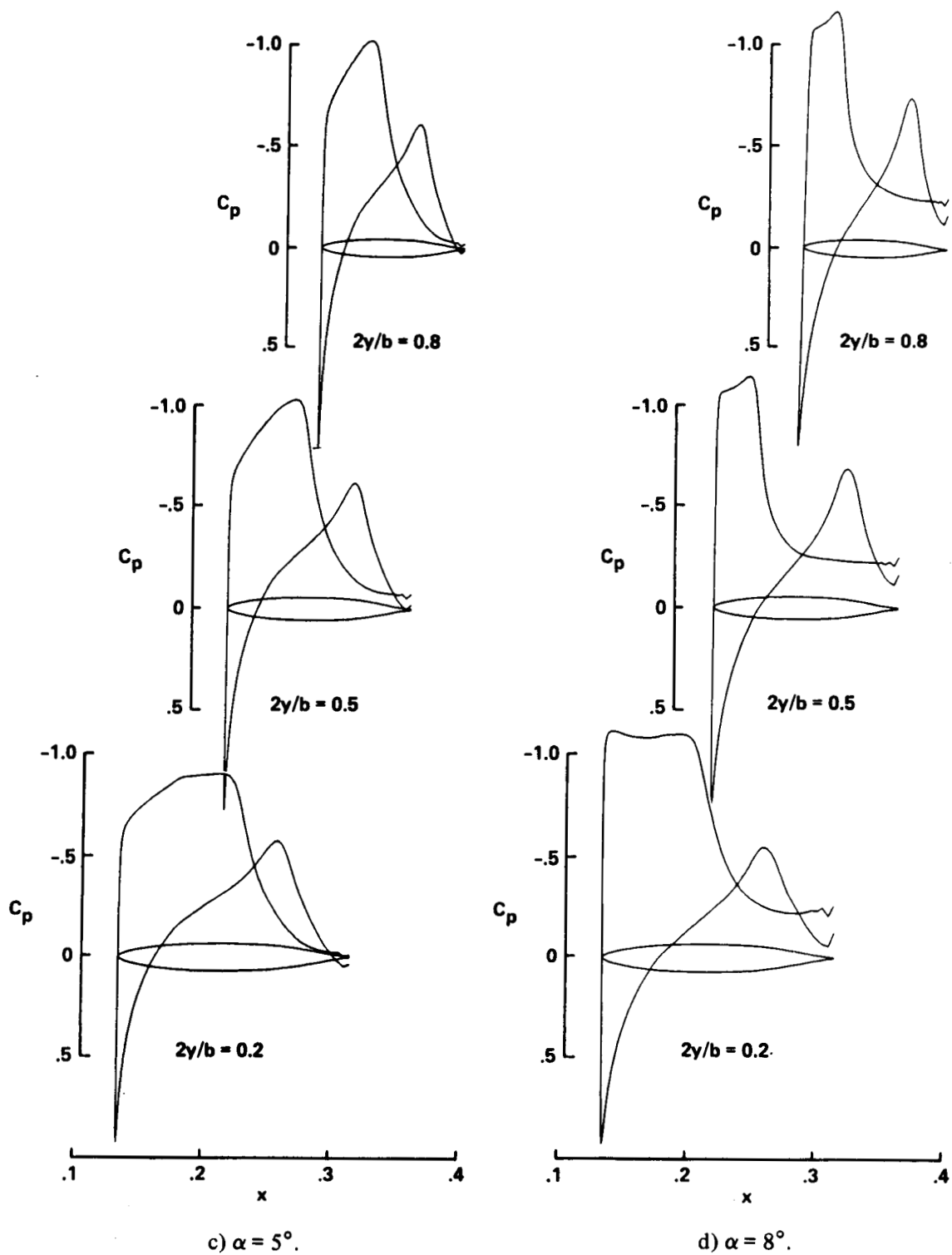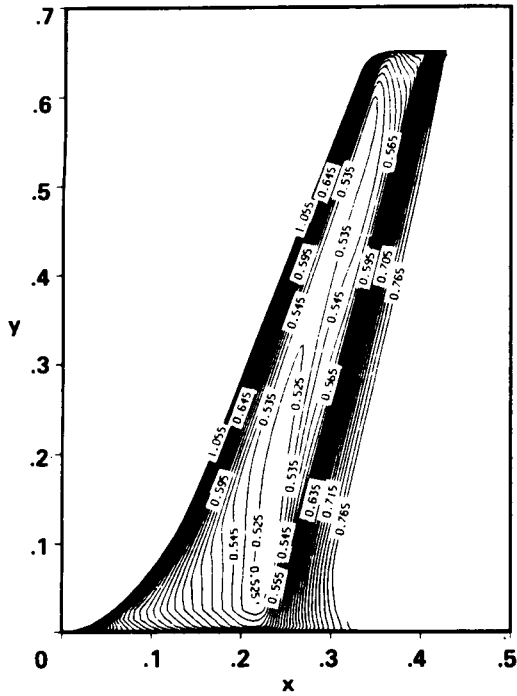
a) $\alpha = 0°$.
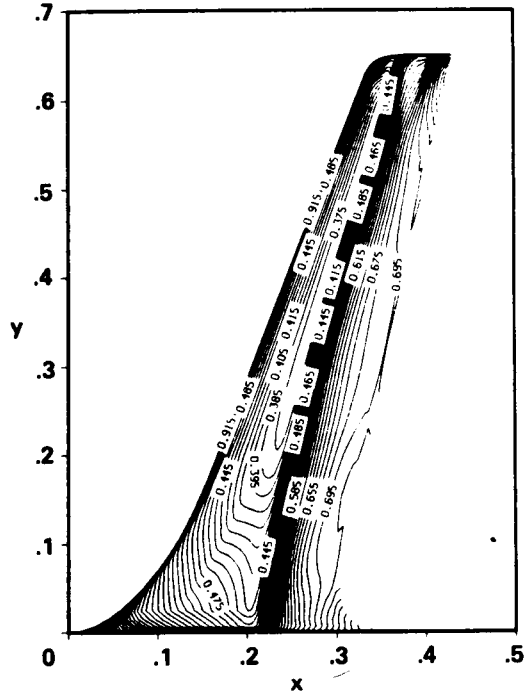
c) $\alpha = 5°$.
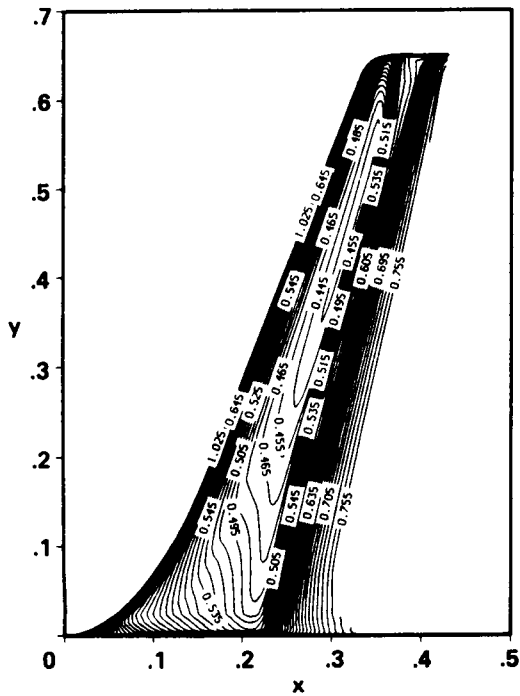
b) $\alpha = 2°$.
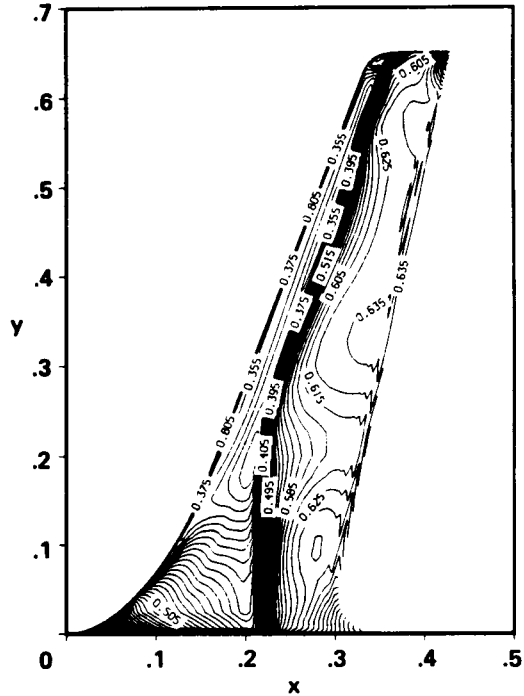
d) $\alpha = 8°$.

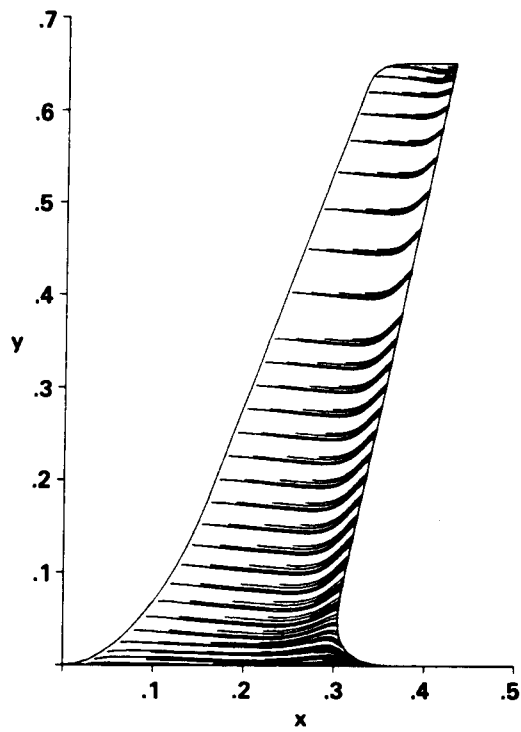Fig. 9 Computed pressure contour plots on upper surface of isolated wing; $M_\infty = 0.82$, $Re = 1.0 \times 10^7$.

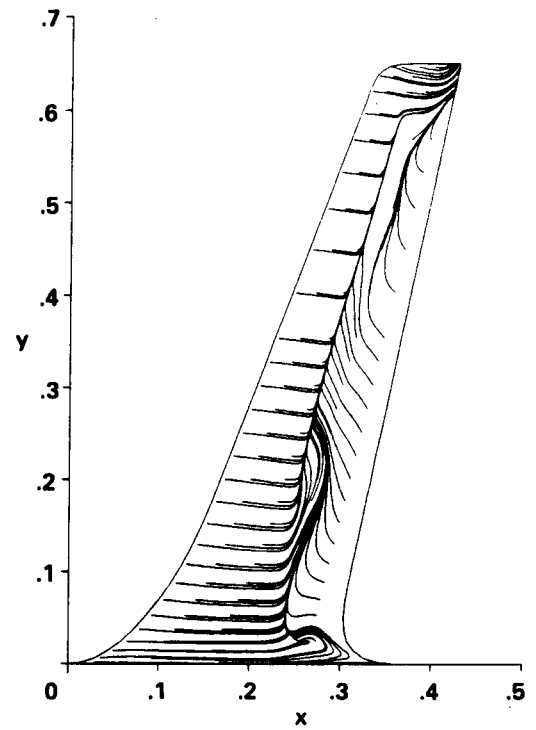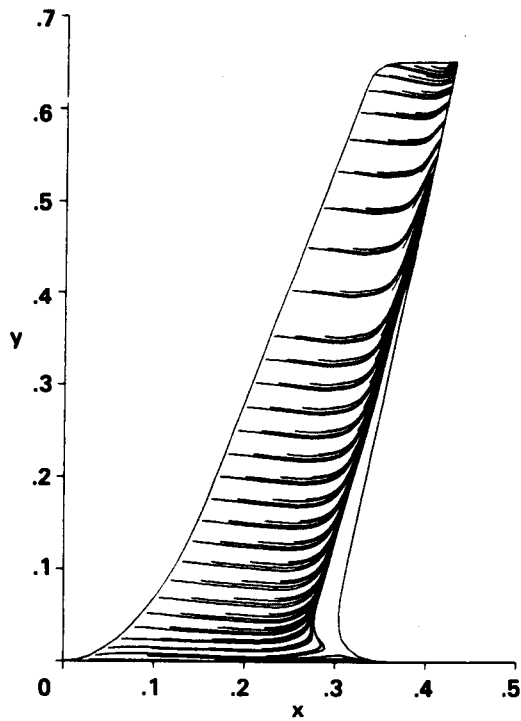a) $\alpha = 0°$.

b) $\alpha = 2°$.

c) $\alpha = 5°$.

d) $\alpha = 8°$.

Fig. 10 Computed surface-flow patterns on upper surface of isolated wing; $M_\infty = 0.82$, $Re = 1.0 \times 10^7$.
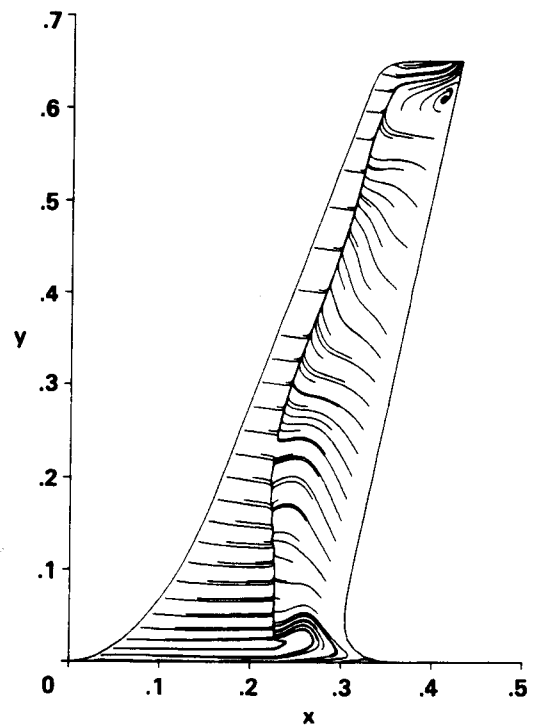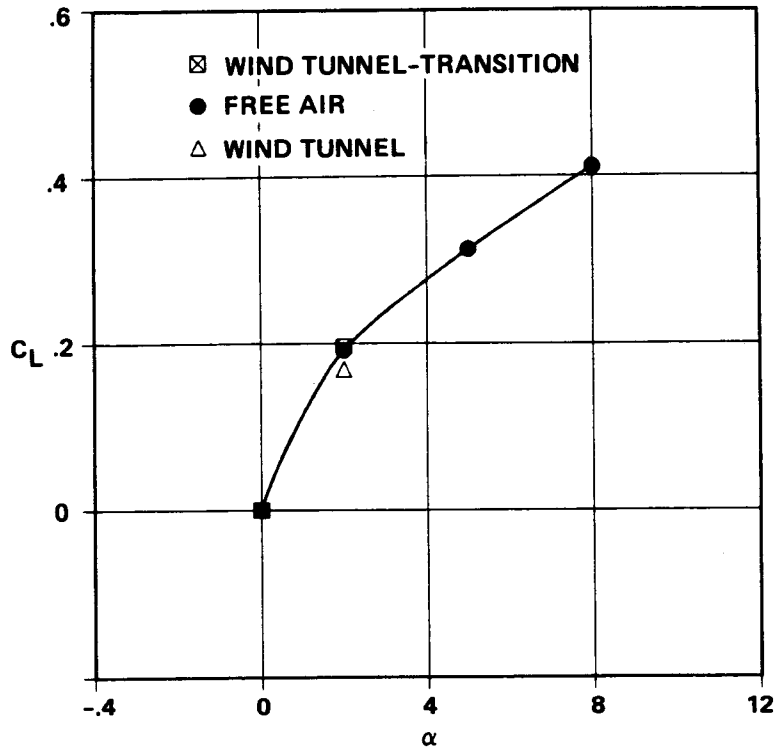
Fig. 11 Lift coefficient versus α; $M_\infty = 0.82$, $Re = 1.0 \times 10^7$.
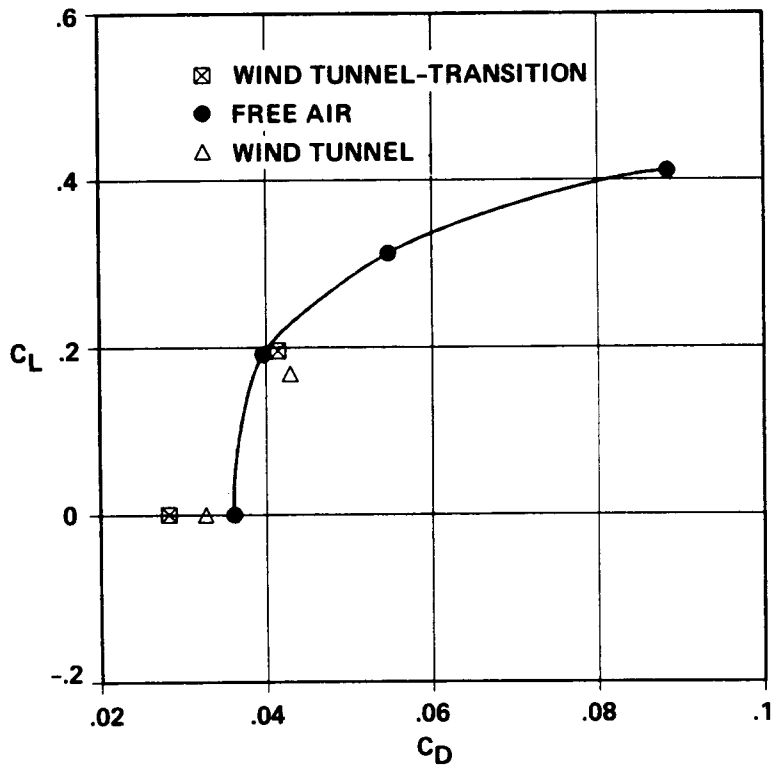
Fig. 12 Lift coefficient versus drag coefficient; $M_\infty = 0.82$, $Re = 1.0 \times 10^7$.

NASA
National Aeronautics and
Space Administration

Report Documentation Page

1. Report No. NASA TM-100042	2. Government Accession No.	3. Recipient's Catalog No.

4. Title and Subtitle	5. Report Date
Navier-Stokes Simulation of Wind-Tunnel Flow using LU-ADI Factorization Algorithm	February 1988
	6. Performing Organization Code

7. Author(s)	8. Performing Organization Report No.
Shigeru Obayashi, Kozo Fujii and Sharad Gavali*	A-88027
	10. Work Unit No. 505-60

9. Performing Organization Name and Address	11. Contract or Grant No.
Ames Research Center, Moffett Field, CA *Amdahl Corporation, Sunnyvale, CA	
	13. Type of Report and Period Covered

12. Sponsoring Agency Name and Address	Technical Memorandum
National Aeronautics and Space Administration Washington D.C. 20546	14. Sponsoring Agency Code

15. Supplementary Notes

Point of contact: Shigeru Obayashi, Ames Research Center, MS 258-1, Moffett Field, CA (415) 694-4473 or FTS 464-4473

16. Abstract

The three-dimensional Navier-Stokes solution code using the LU-ADI factorization algorithm was employed to simulate the workshop test cases of transonic flow past a wing model in a wind tunnel and in free air. The effect of the tunnel walls is well demonstrated by the present simulations. An Amdahl 1200 supercomputer having 128 Mbytes main memory was used for these computations.

17. Key Words (Suggested by Author(s))	18. Distribution Statement
Navier-Stokes Wind tunnel ADI	Unlimited - Unclassified Subject category: 02

19. Security Classif. (of this report)	20. Security Classif. (of this page)	21. No. of pages	22. Price
Unclassified	Unclassified	28	AO-2

NASA FORM 1626 OCT 86